Modeling of a semi-real injection test in sand

Olivier Chupin, Nadia Saiyouri, Pierre-Yves Hicher

Modeling of a semi-real injection test in sand

O. Chupin, N. Saiyouri, P.-Y. Hicher

Research Institute in Civil and Mechanical Engineering (GeM), UMR CNRS 6183, Ecole Centrale de Nantes, BP 92101, Nantes cedex 3, France

This article presents a model of flow and transport with filtration in porous media which is used to analyze large-scale grouting tests. A program based on the finite element method is developed to solve the model equations; a particular attention is paid to inherent issues of transport problems. The analysis of these tests aims at providing insights on the propagation patterns associated to the injection of cement-based grouts in sand. To apprehend particular features that characterize field injections, the experiments are performed by using a tube-a-manchette and a patented grout. Finally, the role of filtration during the tests is discussed.

Keywords:
Grouting
Filtration
Porous media
Balance equations
Finite element method

1. Introduction

This paper presents the modeling of a semi-real injection test in sand. The technique of permeation grouting is used and the effects of filtration on the grout transport are studied. Large scale or in-situ experiments are well suited to examine grouting patterns encountered in fieldworks. However, only few articles in the literature analyze this kind of test. Moreover, articles that deal with in-situ injection tests [35,37] do not focus on the flow and transport phenomena occurring during the grout propagation. On one hand, Tamura and Goto [35] have presented tests in a fine sand layer assumed homogeneous. Typical results concern the injection pressure and the shape of the solidified bodies. Other comments, for instance on the concentration in cement particles (or mechanical properties), are provided but they rely on forensic observations. On the other hand, Tarumi and Sekine [37] have described grouting experiments in sandy soil using long gel time solution type chemicals. The influence of grouting speed on the grouting patterns observed during a test is exposed as well as a method based on pressure charts to control grouting. However, the aforementioned works do not aim at studying filtration and neither conclusion on the importance of this phenomenon during grouting nor simulations of the experiments are discussed. Since cement-based grouts have a particulate nature, the question of filtration during grouting patently arises. Recent studies have focused on the role of filtration during soil injections and a systematical description of fundamental phenomena involved in grouting was first addressed in [6]. In addition, large-scale injection tests in sand are presented in [7] and [9]. Abundant and valuable information about injection pressure, interstitial pressure, grout concentration or displacements of the solid skeleton are provided for these tests which are simulated with a model that includes filtration. Nevertheless, these experiments are not utterly representative of in-situ injections partly because of the injection device used to propagate grout into the soil. In the continuity of existing works, a large-scale experiment performed close to in-situ conditions is presented herein. A sleeved grout pipe and a double packer are used to inject grout into sand. A patented cement-based grout, similar to those manufactured for fieldworks, is utilized. Successive injections are performed from the bottom to the top of the sand specimen. An acoustic method is employed to detect the grout front during the tests and several pressure measurements are recorded. The volumes of injected grout, the injection speeds and dimensions of a solidified bulb are also reported. A model is developed to simulate the tests; its ability to forecast site injections in homogeneous media is evaluated. The analysis of these experiments endeavors to give insights on the importance and the effects of filtration during grouting.

Filtration has a cross-disciplinary interest which has also been manifested in chemical and biological sciences (e.g. [12]). Different kinds of filtration can be distinguished [1,31]; herein the deep bed filtration is considered. It involves particles of small dimensions that are able to propagate within the porous material; some of them are just retained in the medium under mechanical or physicochemical forces [23]. Two distinct mechanisms of filtration are often envisaged. According to Sharma and Yortsos [34], the first one corresponds to the trapping of particles by pore throats whereas the second mechanism reflects the uniform deposit of particles over pore bodies and pore throats causing a gradual reduction of the pore radii. The present article does neither aim to quantify the importance of each local mechanism of particle capture nor to investigate the deposition modes at the microscopic level. Apropos, Kim and Whittle [27,28] have presented a simulation of pore-scale particle deposition and clogging. In the literature, four categories of filtration models can be discerned. These are categorized in [33] as follows: the phenomenological models [23] or continuum models, the trajectory analysis models (e.g. [32]), the stochastic models (e.g. [36]), and the network models (e.g. [19]). A continuum approach is selected in this article. In the context of grouting, the most recent works in this class of methods were proposed by [6] and [33]. Other works on the modeling of the propagation of grouting in soils are presented in [15,24] and [26]; they do not systematically integrate filtration or they deal with chemical grouts. The model developed in [6] considers a single fluid phase transporting miscible components. The filtration is included by considering the adsorption of grout onto the solid matrix. The medium permeability is estimated via a generalized Kozeny–Carman equation. This model depends on four phenomenological equations. One of these is related to filtration and it depends on several coefficients. Among them, the initial deposition rate can be determined only once different evolution laws have been postulated. Beside, the model developed by Saada et al. [33] considers a three phase system where the hydrodynamic dispersion is neglected. The filtration is accounted through mass exchanges between the cement and the skeleton particles. The permeability variation is modeled by a hyperbolic law that depends on the porosity. This law is more appropriate than a Kozeny–Carman type law since it can predict high variations of permeability for low variations of porosity. Capitalizing on the aforementioned works, the model presented in this article extends the continuum methods that express the rate of accumulation of the filtered mass by a kinetics equation [25]. It considers a two phase system; the fluid phase is composed of miscible species. The dispersion flux is thus taken into account for components of this phase. Furthermore, the permeability is estimated through a relation that depends on the concentration of the filtered species [4]. The model depends on two filtration parameters that can be determined from one-dimensional injection tests [14]. It also treats the viscosity and the density variations of the fluid phase.

The mathematical formulation of the presented model is a coupled system of nonlinear partial differential equations. This system is solved by the finite element method with a particular attention to the usual numerical issues inherent to flow and transport problems [17]. Particularly, a smoothing procedure is used to obtain a consistent velocity field and the Streamline Upwind Petrov/Galerkin method [10] enables to avoid numerical diffusion and oscillations in the transport equation. These methods are embedded in iterative procedures used to tackle the coupling between equations of the problem and nonlinearity. Based on the techniques mentioned above, a numerical program is developed by using the Diffpack libraries [30].

2. Mathematical model

The system in consideration is a two-phase porous medium composed of a rigid skeleton and a fluid phase where miscible species are present. Initially, the fluid phase fills the whole pore space such that the medium is saturated. The description of transport phenomena occurring in this system can be obtained from mass balance equations using averaging procedures [2,20]. Starting form the macroscopic balance equations derived by either [2] or [21], a model of transport including filtration is presented herein. For the mathematical purpose, the porous medium is denoted $\Omega \in R^d,\ d = 1, 2, 3$; it has a smooth boundary $\partial\Omega$. The problem is studied over a time period $J = [0, T]$. In this section, the superscript α denotes quantities referring to components of the fluid phase. The superscripts w, c and χ stand for water, transported species (the injected grout in the application to injection) and filtrated species, respectively. The superscript f corresponds to fluid properties.

Let us consider a component transported within the fluid phase. This component is composed of particles and its transport in a porous material is featured by filtration phenomena. From a general point of view, the macroscopic mass balance equation (in the absence of mass transfer across surfaces that delineate system's phases) for a component α of the fluid phase is [21]:

$$\frac{\partial}{\partial t}(\phi\langle\rho^\alpha\rangle^f) + \nabla \bullet (\phi\langle\rho^\alpha\rangle^f\,\overline{v}^\alpha) = \phi\langle\rho^\alpha\rangle^f\,\overline{r}^\alpha, \quad (x,t) \in \Omega \times J. \tag{1}$$

Eq. (1) must satisfy the following condition:

$$\sum_\alpha \phi\langle\rho^\alpha\rangle^f\,\overline{r}^\alpha = 0. \tag{2}$$

In the equations above, $\langle\cdot\rangle^f$ represents the volume-weighted average operator applied to the fluid phase and $\overline{(\cdot)}^\alpha$ is the mass average operator for fluid species. The definition of these operators can be found in [20]. v^α represents the velocity vector of species α, ρ^α the mass density function of species α, r^α the rate of net production of mass of species α as a result of chemical reactions with other species and also due to decay/production processes. Eq. (1) applied to the aforementioned transported component yields

$$\phi\frac{\partial c}{\partial t} + \nabla \bullet (cq) - \nabla \bullet (D^c\nabla c) = \phi c\overline{r}^c = -\lambda|q|c, \quad (x,t) \in \Omega \times J, \tag{3}$$

where c is the concentration of the transported component (average signs omitted, c is a macroscopic quantity) and q is the specific discharge given by the generalized Darcy law (momentum balance equation),

$$q = \phi(\overline{v}^f) = -\frac{k}{\mu^f}(\nabla p - \langle\rho\rangle^f g), \quad (x,t) \in \Omega \times J. \tag{4}$$

$\overline{v}^f$ represents the fluid velocity with respect to a fixed coordinate system, k is the permeability tensor, μ^f is the fluid viscosity, and ρ^f is the fluid density. D^c is the hydrodynamic dispersion tensor that characterizes the spreading of particles at the macroscopic level resulting from mechanical dispersion and molecular diffusion. According to the relation proposed by Bear [2],

$$D^c = \phi(D^c_m + D^c_d) = a_T|q|I + (a_L - a_T)\frac{q \otimes q}{|q|} + \phi D^c_d T, \quad (x,t) \in \Omega \times J, \tag{5}$$

this tensor is a function of the specific discharge in the medium and it depends on two parameters: a_L and a_T are the longitudinal and the transversal dispersion coefficients, respectively. D^c_d is the molecular diffusion coefficient and T is the tortuosity.

Filtration is introduced in Eq. (3) through the degradation term (r.h.s. of Eq. (1)). A common relation for this term is [3]:

$$\phi\langle\rho^\alpha\rangle^f\,\overline{r}^\alpha = -\phi k_{cf} c = -\lambda|q|c, \quad (x,t) \in \Omega \times J. \tag{6}$$

This sink term expresses the rate of disappearance of the component α. The withdrawn component is at concentration c which corresponds to the concentration of the transported species at this location. $k_{cf}\,[T^{-1}]$ is a degradation rate parameter for the component in the fluid phase. The later parameter is expressed as the product of the filtration coefficient, λ $[L^{-1}]$, and the specific discharge of the fluid phase. The rate of accumulation of the filtered mass is expressed by the kinetic equation,

$$\phi \frac{\partial \chi}{\partial t} = \lambda |q| c, \quad (x,t) \in \Omega \times J. \tag{7}$$

χ is the concentration of the filtrated species. Eq. (7) can also be interpreted as a mass balance equation for the filtered species. According to Sharma and Yortsos [34], the species to be considered when referring to filtration mechanisms are the suspended particles, the attached particles and the trapped particles. Let us assume that the filtrated particles are not attached to the solid matrix but rather trapped within the pore space. A filtrated component is then defined; it is expressed as a mass per pore volume. This component acts as it belongs to the fluid phase but resting in a stagnant state. According to Bear [3], part of a liquid phase may be immobile or stagnant. This part is in direct contact with the mobile portion enabling the transfer of mass from one to the other. Here, the stagnant part is not treated as a separated phase but as a component of the global fluid phase. This component is nothing but χ. As a consequence the porosity of the medium can be taken constant as long as the solid skeleton is rigid. The r.h.s term of Eq. (1) becomes a source term for the filtrated component and must be equal (absolute value) to the sink term of Eq. (3) according to Eq. (2). The velocity of a component of the fluid phase is the sum of a macroscopic dispersion velocity and the mean velocity of the fluid phase [21]. As long as the filtrated component is considered, the dispersion velocity is assumed to balance the average fluid motion. The null velocity for the filtered species is thus ensured.

The pore pressure (p) can be determined from the total mass balance of the fluid phase,

$$\phi \beta_p \frac{d^f p}{dt} + \phi \sum_i \beta_i \frac{d^f c_i}{dt} + \nabla \bullet q = 0, \quad (x,t) \in \Omega \times J, \tag{8}$$

which is also called flow equation. $d(\cdot)/dt$ is the material derivative defined by: $d()/dt = \partial()/\partial t + \overline{v}^f \cdot \nabla()$. Since mass exchanges involve only the transported and the filtrated components of the fluid phase, additional terms due to filtration do not appear in Eq. (8). The equation of state for the fluid phase density,

$$\langle \rho \rangle^f (x,t) = \rho_0^f \exp(\beta_p (p - p^0) + \sum_i \beta_i (c_i - c_i^0)), \quad (x,t) \in \Omega \times J, \tag{9}$$

used to obtain the flow equation depends on the pore pressure and on the concentration of the components that belong to this phase. Temperature effects are neglected. The summations in Eq. (8) and Eq. (9) are performed over the number of components within the fluid phase. Thus, c_i represents either the transported (c) or the filtrated (χ) concentration depending on i. β_p is the coefficient of compressibility at constant concentration. β_i denotes the coefficient of concentration that introduces the effect of $\langle \rho \rangle^f$ change as a result of a change in concentration of either the transported or the filtrated component at constant pressure.

As mentioned earlier, the filtration phenomenon is responsible for a decrease of the medium permeability. This reduction is modeled by a hyperbolic law,

$$k(x,t) = \frac{k_0}{1 + \beta \chi}, \quad (x,t) \in \Omega \times J, \tag{10}$$

which depends on the concentration of the filtrated component. Eq. (10) was already utilized by Bedrikovetsky et al. in the analysis of filtration in seawater core-flood experiments. In the context of grouting, Saada et al. [33] used a similar function of the filtration-induced porosity change to model variations of permeability. β is a filtration coefficient referred as the damage coefficient; it can be determined experimentally. k_0 represents the initial permeability of the medium.

Finally, the evolution of the dynamic viscosity,

$$\mu^f (x,t) = \left(1 - \frac{\mu_0}{\mu_c}\right) \frac{c}{\rho^c} + \mu_0, \quad (x,t) \in \Omega \times J, \tag{11}$$

is assumed to vary linearly with the concentration of the transported component. μ_0 is the initial viscosity of the fluid phase and μ_c is the viscosity of the invading fluid. ρ^c represents the density of the transported component.

If the Oberbeck–Boussinesq assumption is made (density dependencies are considered only in the buoyancy term of Darcy's law), the dispersion and the viscosity variations are neglected, then the presented model reduce to a classical filtration model as presented in [4].

3. Numerical approach

The mathematical model is represented by a system of nonlinear partial differential equations (PDE's). The coupled set of initial-value PDE's is expressed in the general form:

$$L(u) = m^T \frac{\partial (g^T u)}{\partial t} + \nabla \bullet (f) - b = 0, \quad (x,t) \in \Omega \times J, \tag{12}$$

where $L(u)$ is a differential system written in terms of the state variables $u(x,t)$. Appropriate boundary conditions along $\partial\Omega$ and an initial condition on $\Omega \cup \partial\Omega$ are required to compute a solution. In Eq. (12) the following definitions are used:

$$u = \begin{Bmatrix} p \\ c \\ \chi \end{Bmatrix}, \quad g = \begin{Bmatrix} 1 \\ 1 \\ 1 \end{Bmatrix}, \quad m = \begin{Bmatrix} \phi \beta_p \langle \rho \rangle^f \\ \phi \\ \phi \end{Bmatrix}, \quad f = \begin{Bmatrix} \langle \rho \rangle^f q \\ cq - D^c \nabla c \\ 0 \end{Bmatrix},$$

$$b = \begin{Bmatrix} -\phi \langle \rho \rangle^f \sum_i \beta_i \frac{\partial c_i}{\partial t} \\ -\lambda |q| c \\ \lambda |q| c \end{Bmatrix}. \tag{13}$$

The problem is discretized in time by finite differences using the classical trapezoidal rule (or θ-rule) and discretized in space by the finite element method. The θ-rule applied to Eq. (12) reads:

$$m^T \frac{(g^T u)_{n+1} - (g^T u)_n}{\Delta t} = -(\theta \nabla \bullet (f_{n+1}) + (1-\theta) \nabla \bullet (f_n)) + \theta b_{n+1} + (1-\theta) b_n. \tag{14}$$

$\theta = 1$ yields the implicit scheme (first order accurate in time), $\theta = 1/2$ is the Crank–Nicolson scheme (second order accurate in time) and $\theta = 0$ is the explicit scheme (first order accurate in time). In the following θ, is set to 0.5. n represents the time level and Δt is the time step increment. The finite element formulation of Eq. (14) leads to a discrete coupled system of nonlinear equations that can be written as follows:

$$F_{n+1} = A(U_{n+1}) U_{n+1} - B = 0, \quad U_{n+1} = \begin{Bmatrix} p_{n+1} \\ c_{n+1} \\ \chi_{n+1} \end{Bmatrix}. \tag{15}$$

U_{n+1} is the vector that contains the discrete state variables.

Two basic strategies can be applied for the resolution of such a system: either one solves Eq. (15) in sequence with an outer iteration or one applies a standard nonlinear method (e.g. Newton–Raphson method) to the compound system. In the second case, the solution is searched for all the variables, p_{n+1}, c_{n+1} and χ_{n+1}, simultaneously. The convergence of the Newton–Raphson method is quadratic. However, a decoupled strategy is chosen instead of a fully implicit method herein for its computationally efficiency and appropriateness for large scale problems. Moreover, the system to be solved can be ill-conditioned by using fully implicit methods if the scales of phenomena involved in the problem are significantly different [17]. The Gauss–Seidel-type and the Jacobi-type algorithms for systems of nonlinear PDE's are selected. The attractive feature of these iterative approaches is that only standard PDE's needs to be solved. If the transport equation is denoted F^c, the pressure equation F^p and the filtration equation F^χ, then the Gauss–Seidel-type algorithm can be expressed as in Fig. 1 where k represents the iterative index. First, the flow equation is solved with respect to p by considering the other state variables at the previous iteration, $k-1$. Thereafter, the concentration and the filtration equations are solved according to c and χ, respectively, by using the most recently computed state variables (i.e. at iteration k). The Jacobi method is comparable to the Gauss–Seidel approach except for the solving of the transport and the filtration equations: these are solved by considering the main variable at iteration k but the other variables at the previous iteration, $k-1$.

The decoupled equations obtained after application of the Gauss–Seidel-type or the Jacobi-type methods can be still nonlinear with respect to their own main variables. In that case, the Picard iterations [38] are preferred again to the Newton–Raphson method because the quadratic convergence for the global system is lost since the decoupled strategy has been utilized to handle Eq. (15). In the following, the Picard method is exemplified on the flow equation but it can be applied in the same way to other equations. The Picard iterative scheme for the decoupled pressure equation is:

$$p_{n+1}^{k,i} = [A^p(p_{n+1}^{k,i-1})]^{-1}(B^p)_{n+1}^{k,i-1}. \tag{16}$$

In Eq. (16), superscript i denotes the current iterative index of the Picard iterations and subscript $n+1$ stands for the current stage of the global system. A given initial guess p_0 is needed to launch the Picard method. This guess is set equal to the pressure field computed at the previous time. The iteration procedure is terminated once a convergence criterion is satisfied. A deviatoric error measure in form of

$$\|U_{n+1}^k - U_{n+1}^{k-1}\|_{L_p} < \delta, \tag{17}$$

is adopted. δ is a chosen error tolerance and L_p identifies the error norm.

Note that the transport equation requires specific solving methods when advection is dominant over diffusion (i.e. for high Peclet numbers). In point of fact, the use of the classical Galerkin discretization in that particular case corrupts the solution with spurious oscillations and numerical diffusion. This issue is overcome by utilizing the Streamline Upwind/Petrov–Galerkin (SUPG) method [10] that consists in selecting weighting functions apart from the basis functions in the variational formulation of the problem.

Another important point concerns the velocity approximation. Indeed quoting [17], "in Darcy's law the discretization of the fluxes q is nontrivial if the density effects become important. Specifically, a lower-order approximation attainable for the pressure gradient ∇p can conflict with a higher-order spatial variation in the gravity term ρg. This situation can be encountered when the pressure and the concentration are approximated based on the same order of polynomials". Consequently, the Moving Least-Squares (MLS) smoothing technique is applied to velocities in order to obtain a consistent field free of numerical artifacts. It turned out that this procedure was essential to recover the solution of the Elder benchmark (see below) used to validate the developed program. The MLS technique consists in fitting a linear or quadratic polynomial to the discrete values of a finite element field.

Given guesses p_{n+1}^0, c_{n+1}^0 and χ_{n+1}^0 for the solutions of $F_{n+1}^p(p_{n+1}, c_{n+1}, \chi_{n+1}) = 0$, $F_{n+1}^c(p_{n+1}, c_{n+1}, \chi_{n+1}) = 0$ and $F_{n+1}^\chi(p_{n+1}, c_{n+1}, \chi_{n+1}) = 0$

1. update k
2. solve $F_{n+1}^p\left(p_{n+1}^k, c_{n+1}^{k-1}, \chi_{n+1}^{k-1}\right) = 0$ with respect to p_{n+1}^k
3. solve $F_{n+1}^c\left(p_{n+1}^k, c_{n+1}^k, \chi_{n+1}^{k-1}\right) = 0$ with respect to c_{n+1}^k
4. solve $F_{n+1}^\chi\left(p_{n+1}^k, c_{n+1}^k, \chi_{n+1}^k\right) = 0$ with respect to χ_{n+1}^k
5. check convergence criterion

Fig. 1. Gauss–Seidel-type algorithm for the coupled system.

The methods stated above constitute the basis of a global solving process which involves different embedded iterative procedures occurring at the coupling level and at the nonlinear level of the decoupled system. The global algorithm is programmed by using the Diffpack libraries [30] which provide numerous modules (e.g. mapping of FE problems) so that the developer can essentially focus on the variational formulation of a problem, the solving strategy, etc. As recommended in [30], different C++ classes are built to represent each physical phenomenon. Basically, the transport, the flow and the filtration equations are implemented in separated classes. These classes take advantage of the inheritance properties of the C++ language to derive subclasses relative to the implementation of the nonlinear and the coupled aspects of the problem. The coupling between the equations of the problem is managed by another class as well as the common constitutive relations. The Diffpack libraries were also used by Bouchelaghem [8]. The developed program was validated on the Henry [22] and the Elder [18] benchmarks which deal with variable density flow and transport in aquifers. They enable to verify the coupling between the equations and the nonlinear solver on a 2D problem. The analysis of these benchmarks proved that the program is robust and that it can accurately handle the bifurcation in the Elder problem. To recover the bifurcated solution of the Elder problem, the velocity field of the fluid phase must be computed accurately. The MLS technique turns out to be essential to achieve such a result. Moreover, the Elder problem is a large scale problem (domain: 600 m by 150 m) studied over a long time period (20 years). To obtain a solution in a reasonable time limit, iterative methods for solving the linear systems are required. As long as the system into consideration is symmetric and positive definite the conjugate gradient (CG) method associated to a Relaxed Incomplete LU factorization (RILU) preconditioner is convenient. For nonsymmetric systems, the choice is not straightforward. Several methods have been tested before selecting the BIConjugate Gradient Stabilized (BICGS) procedure joined together with a RILU preconditioner. The resolution time obtained for the Elder problem meshed with a very fine grid (9900 elements) and studied over a period of 20 years was 4996 min while using a Pentium III 864 MHz computer. As an indication, the resolution time for the simulation presented in Section 4 is about 16 min. Once the global algorithm was verified, the program part that deals with filtration was tested on an analytical solution computed in a simplified case. More details on the validation procedure are presented in [13].

4. Analysis of large-scale injection tests

The details of the large-scale injection tests are presented in this section. The tests are performed under conditions close to in-situ conditions; particularly, a sleeved grout pipe (or tube-a-manchette) is used to inject the grout into the soil. On site injections are performed by utilizing this engineering device [29] and according to Cambefort [11] this is the only way to easily achieve injection of gravels and sands. The experiment is conducted in collaboration with VSL-Intrafor Soletanche and EuroPhysical Acoustic companies. It aims at studying a three-dimensional injection case and grouting patterns inherent to fieldwork injections. A simulation of the test is also described in this section and the influence of filtration is discussed.

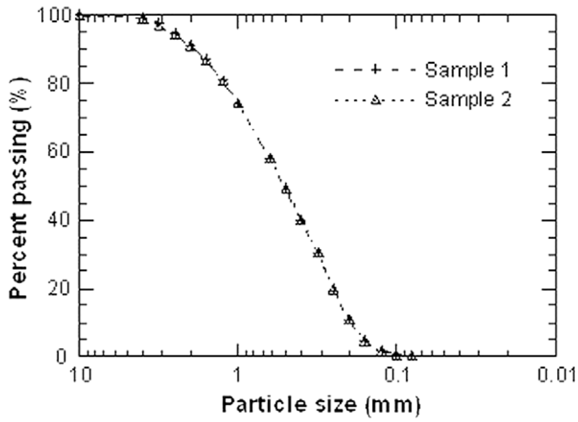

Fig. 2. Grading curve for the Loire river sand.

The experiment consists of injecting cement grout in a cylindrical tank of height 6.0 m and 3.0 m in diameter filled with Loire river sand whose properties are given in [16]. The grading curve of this sand is plotted in Fig. 2. The Loire river sand is composed of sub-rounded particles and elongated shell fragments. The sand is deposited in the tank by successive layers and a fixed density is obtained by tamping each layer. A pluviation technique cannot be used because of the initial moisture content of the sand. The dry density of the sand after tamping is 1.6 (measurements in several layers using calibrated cupels) and a calculation performed, a posteriori, on the whole sand sample evaluates the density at a value of 1.65. The porosity of the resulting specimen is estimated at 0.3. During the filling phase, a cylindrical tube (0.1 m in diameter) located in the center of the tank enables to maintain a volume free of sand for the positioning of the sleeved grout pipe. The latter (17 tube elements of length 0.33 m) is inserted in this aperture after the tank is entirely filled up with sand. The sleeved grout pipe is sealed to soil by pouring casing grout (cement bentonite) in the aperture. The cylindrical tube is removed before the casing grout has hardened. By reserving space into the specimen, no drilling operation is needed to set up the sleeved grout pipe. Note that the casing grout (or sleeve grout) has a low C/W ratio so it can be fractured easily under the injection pressure; then, the grout can propagate through the cracks.

The patented grout formulated for the test is composed of very fine cement (Spinor A12), water, a plasticizer additive and an inert charge in order to increase the fluidity and the stability of the grout [5]. The diameter of cement particles is lower than 12 μm and media with permeability below 10^{-4} m/s can be injected with this grout. The grout density is equal to 1.36 and its viscosity, which has been measured with a rheometer, is equal to 4.15×10^{-3} Pa s.

In order to measure the pore pressure in the sample during injection, six piezometers are vertically placed into the soil at different depths and radial distances from the tube-a-manchette (Fig. 3). The piezometric levels are transcribed by an electric probe that indicates on a ruler the height of water in a piezometer tube. The overpressure due to grouting is deducted from the piezometric statements. In fact, the static piezometric level can be estimated from the starting level (prior to injection) and the volume of injected grout. Then, the overpressure is obtained by subtracting the static level to the measured piezometric level during grouting. The injection pressure at the pump outlet, the volume of injected grout and the injection rate are also recorded during a test.

Measurements of acoustic emission (AE) are performed. They aim to follow the grout propagation during the injection process by recording acoustic activity within the soil specimen. The acoustic activity is sensed through wave guides connected to transducers (type R15 with a maximum frequency resonance of 150 kHz). The wave guides are cylindrical aluminum rods. Two of them, WG2 and WG3, are horizontally inserted into the sand specimen through windows 2 (z = 1.3 m) and 3 (z = 2.1 m) (Fig. 3). The radial distance from the sleeved grout pipe to WG3 and WG2 is 0.4 m and 0.6 m, respectively. An increase of the acoustic emission is expected when the grout reaches a wave guide. This behavior was notably noticed during preliminary tests in columns and small tanks conducted to calibrate the method.

Five injections are performed through five sleeves: S3, S4, S6, S12, S14; the experimental set up is illustrated in Fig. 3. Prior to the grouting phase, the sand is saturated with water. This is accomplished in two times and the water level before injections through S3, S4 and S6 is about 2.55 m (from the bottom of the tank). This

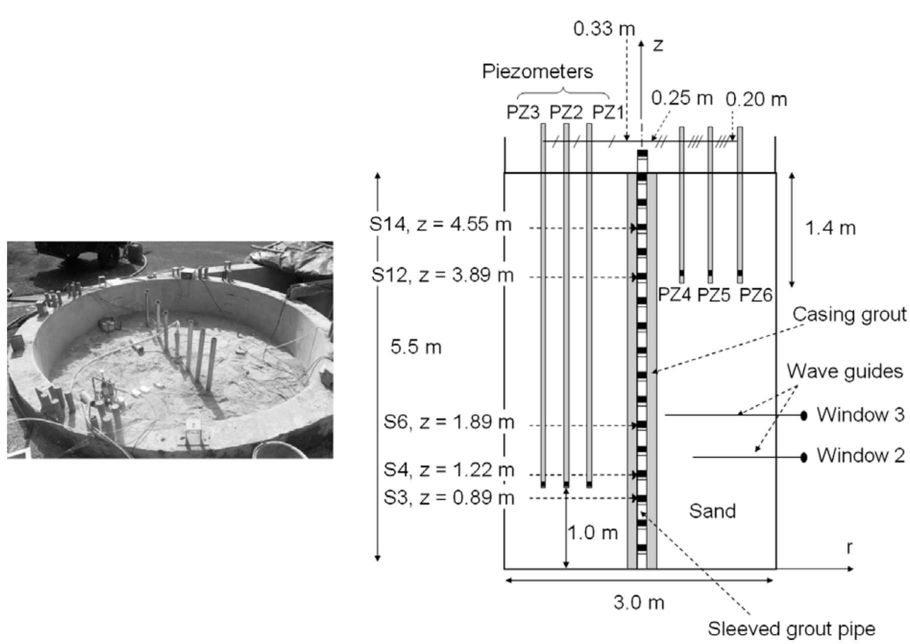

Fig. 3. Description of the experimental set-up.

level is at 4.9 m prior to injecting grout through S12 and S14. The volume of injected grout and the injection rates are given in Table 1. During injections through S12 and S14, grout resurgences appeared at the ground surface. Therefore, the injections were stopped prematurely (see Table 1).

During the injection of S3, S4 and S6, the pressure measured at the outlet of the pump (Fig. 4a) exhibits few brutal drops whereas an increase or at least constant values are expected. Indeed, the pressure is supposed to continuously increases as a function of the injected volume. After a drop, the pressure comes back to a normal level. The low pressure regime observed during these tests is assumed to occur when the fluid pressure is higher than the stability limit of the soil. The soil structure locally collapses and as a result the grout can propagate at low pressure. Moreover, it has been proposed in the past that fracturing pattern is correlated to a pressure reduction during injection. According to Tarumi and Sekine [37], fracturing grouting and permeation grouting can coexist at the same time. Herein, the pressure measured before a significant drop is about 110 kPa and the injection rate is lower than 6 L/min. Concerning the injection through S3, a pressure drop is noticed 125 min after the injection has started. A drop appears after 15 min in the case of S4 and S6.

Table 1
Characteristics of the different injections.

	S3	S4	S6	S12		S14
Volume of injected grout (L)	553	350	344	98	18	58
Injection rate (L/min)	3.52	4.67	5.92	4.25	1.92	5.92
Injection duration (min)	157	75	58	23	9	10

Table 2
Parameter values used in the simulation.

Sand density	18.16 kN/m^3
Porosity	0.3—————
Permeability	1.75E−11 m^2
Grout C/W ratio	0.36
Grout density	1360 kg/m^3
Grout viscosity (rheometer)	4.15E−3 Pa s
Specific discharge	7.15E−4 m/s
Longitudinal dispersion coefficient	1.0E−2 m
Transversal dispersion coefficient	1.0E−3 m
Molecular dispersion coefficient	1.0E−10 m^2/s
Transported concentration coefficient (β_c)	2.65E−4———
Filtrated concentration coefficient (β_χ)	6.59E−4———
Coefficients of filtration: (λ, β)	(0.0252 m^{-1}, 3.66E−2 m^3/kg)

The pressure needed to break the casing grout is usually an instantaneous value that decreases rapidly once the casing is cracked. Herein, no peak is observed during the water injection (saturation phase). The pressure recorded behind the sleeve during the saturation phase is nearly constant and equal to 75 kPa. Concerning the grout injections, the pressure raise is not instantaneous but is spread over 2–3 min. This pressure is then defined as a starting injection pressure rather than a fracturing pressure required to cracking the casing grout.

The evolution of the hydraulic head during the experiments is measured by piezometers. Fig. 4b shows this evolution with time for the injections through S3, S4 and S6. The overpressures resulting from these measurements are small (less than 2 kPa) and almost the same for all the piezometers, independently of the distance from the injection source. Bouchelaghem [9] noticed a similar trend, i.e. that most of overpressures occur in the vicinity of the injection tube.

Fig. 5 displays the acoustic activity recorded for WG3 and WG4 during the injection through S6. Expectedly, WG3 exhibits first an increase of the AE activity since it is located closer to the injection source than WG2. WG3 and WG2 detect successively a modification of the AE activity in the soil specimen at times $t = 200$ s and $t = 250$ s. Note that the AE activity must be correlated to the grout arrival upon a wave guide. Consequently, the position of the grout front for injection S6 is supposedly known at times $t = 200$ s and $t = 250$ s. However, WG4 is at a radial distance of approximately 0.84 m from S6 so it is unlikely that the grout reach WG4's end after 250 s. For instance, a simple calculation that considers a spherical injected area without dispersion or dilution (spherical model) predicts the arrival of the grout on WG4 after 125 min (for an injection rate equal to 5.92 L/min). Two main reasons are advanced to explain the early increase of AE activity experienced by WG4: (i) grout propagates through a preferential path possibly created during the previous injections (S3 and S4) as a result of the fracturing patterns observed. (ii) Grout interacts with the injected area stemming from the injection through S4. More generally, AE measurements can also be disrupted by external noises. The detection through WG3 seems more plausible and is discussed in the comparison with the simulation.

Once the five injections are performed and the grout has hardened (more than 28 days after the injections), the solidified bodies resulting from injections S12 and S14 are removed from the soil specimen. All the solidified bulbs are not dug up because of the difficulty to reach the injected aggregates located at the bottom of the tank. The dimensions of the bulb formed during the injection

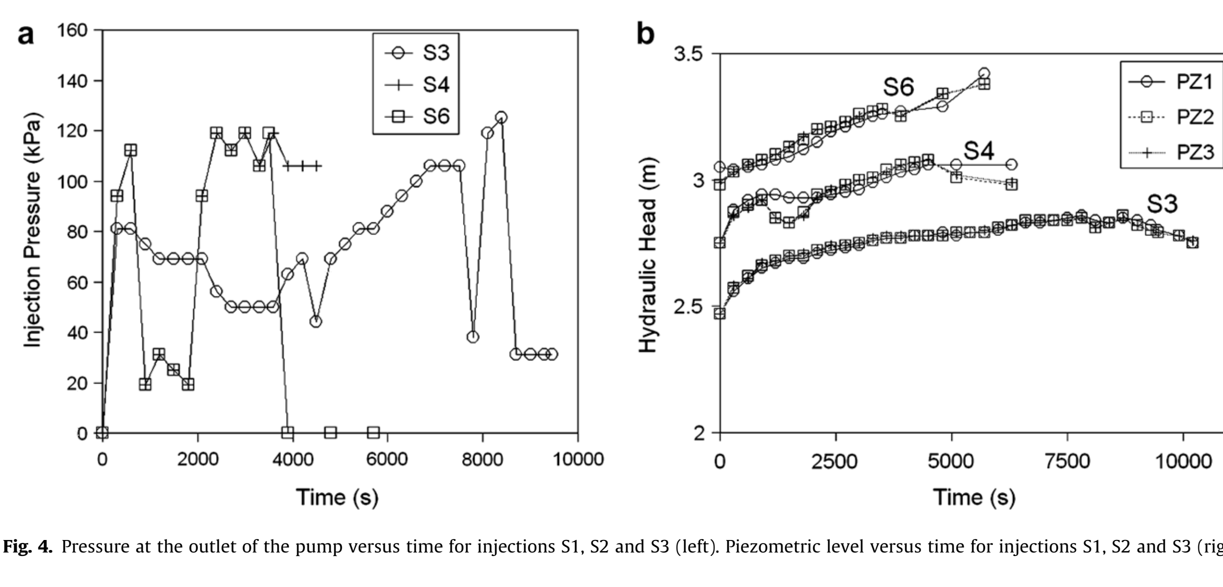

Fig. 4. Pressure at the outlet of the pump versus time for injections S1, S2 and S3 (left). Piezometric level versus time for injections S1, S2 and S3 (right).

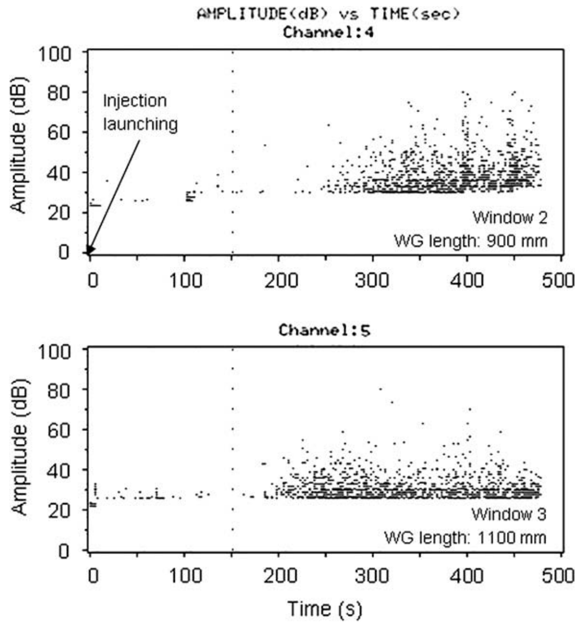

Fig. 5. Acoustic activity recorded by WG2 (up) and WG3 (down) for the injection through S6.

through S12 are drawn in Fig. 7. The grouted bulb is asymmetric essentially because of the grout flow that was observed along piezometer PZ4 during the grouting phase. However, the part of the solidified bulb on the "left" of the tube-a-manchette has a regular shape (Fig. 7). The soil has been permeated without anomaly in this area. This shape is almost spherical; the dimensions of the horizontal cross section are just slightly different in the r and normal to r directions. This part of the bulb is considered to be representative of the injection through S12. As an indication, the volume of grout injected through S12 corresponds to a soil volume of 0.39 m^3. Assuming a spherical volume, the radius of the grouted soil is equal to 0.45 m which is close to the dimensions of the "left" part of the bulb displayed in Fig. 6. The difference may be explained by dispersion (and diffusion) effects that causes the dilution of the grout front during the propagation stage or by small a small anisotropy of the soil characteristics.

The simulation of injection S6 is presented below. This experiment is selected for the comparison with the numerical model because it allows the confrontation with AE measurements. The simulation is performed considering axisymmetric conditions. A constant inflow rate is imposed on a segment of height approximately a sleeve height which matches the mesh element size, i.e. 0.11 m. The z-coordinate of this segment is 1.87 m. The domain is discretized by 50×15 elements of equal dimensions and the time step is set to 100 s. Table 2 summarizes values of the parameters used in the simulation. Boundaries of the domain are enforced with no flux conditions except on the upper boundary where the relative pressure is imposed to zero and on the segment subjected to a constant inflow rate (injection source). The filtration parameters are determined from one-dimensional injection tests which were performed considering the same materials and an analytical solution of the 1D problem under some assumptions [14]. The results are analyzed regarding to the pore pressure and the concentration of the transported and the filtrated components. The numerical results are compared to the experimental data in terms of pressure and AE measurements.

Fig. 6 shows the concentration of the transported grout at times $t = 200$ s, $t = 300$ s and $t = 3500$ s which corresponds approximately to the end of the experiment. The time $t = 3500$ s can be used to

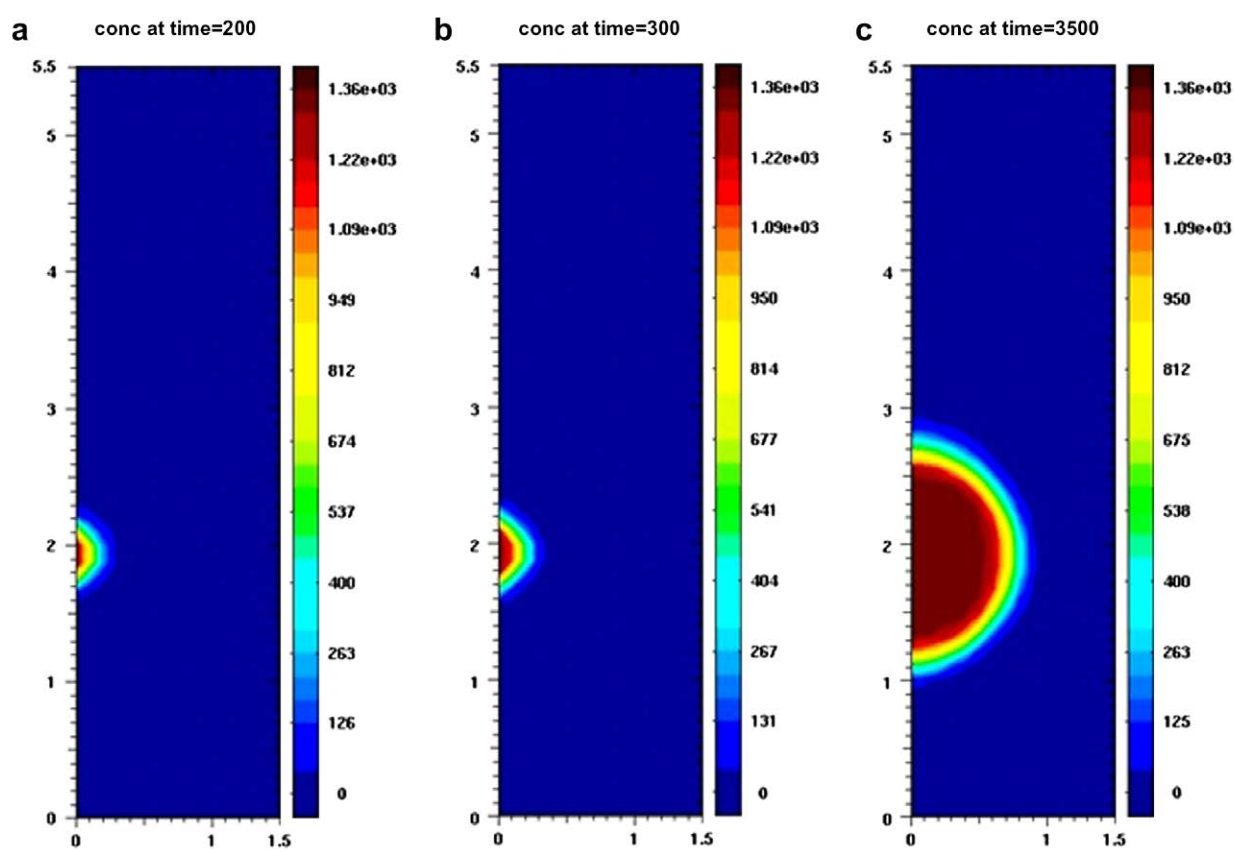

Fig. 6. Concentration of the transported component (kg/m^3) at different times (s).

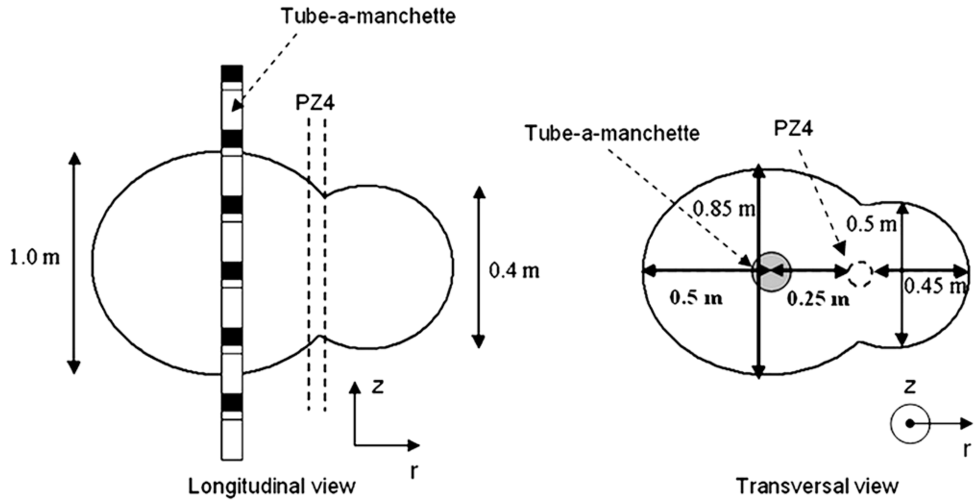

Fig. 7. Longitudinal and transversal views of a solidified bulb (injection S12).

estimate the dimensions of the solidified bulb obtained after hardening of the grouted mass. The regions of the injected mass where the concentration is low do not harden properly and do not contribute to the formation of a solidified bulb. Besides, Bouchelaghem [9] considered that only the domain with a concentration at least equal to half the density of the injected grout can be retained in the determination of the bulb dimensions. The grouted region obtained numerically is quasi spherical, and by making the same assumption as Bouchelaghem [9] the radius of the solidified bulb is estimated at about 0.7 m. The same simple calculation as done previously (spherical injected mass plus no dispersion) predicts a radius of 0.65 m. The difference between these two values is small and can be explained by the dispersion effects which are included in the model. A similar difference was noticed above between this simple calculation and the excavated bulb stemming from injection S12. The concentration at time $t = 200$ s is confronted to the AE measurement obtained from WG3. This wave guide detects an increase of the AE activity 200 s after the injection has started. Numerically, the grout front (limit between zero and nonzero concentrations) is in $r = 0.3$ m at this time. WG3 is located at $r = 0.4$ m and hence catches an increase of the acoustic activity before the numerical concentration reaches the wave guide. A precision has

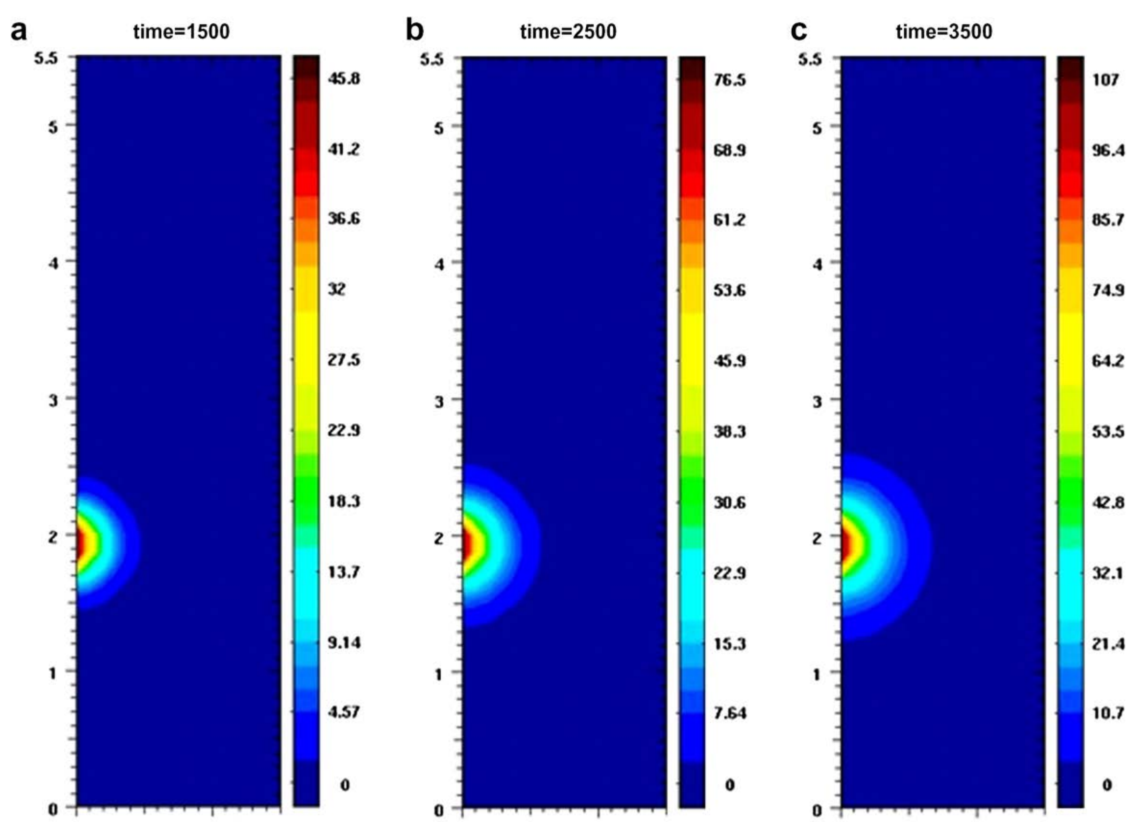

Fig. 8. Concentration of the filtrated component (kg/m^3) at different times (s).

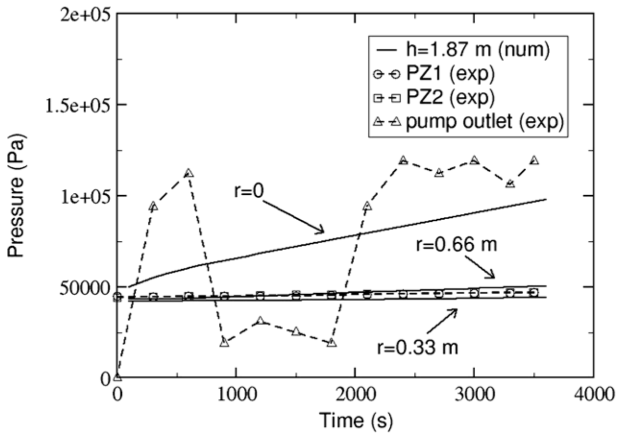

Fig. 9. Evolution of the pore pressure versus time at different locations (experimental and numerical results).

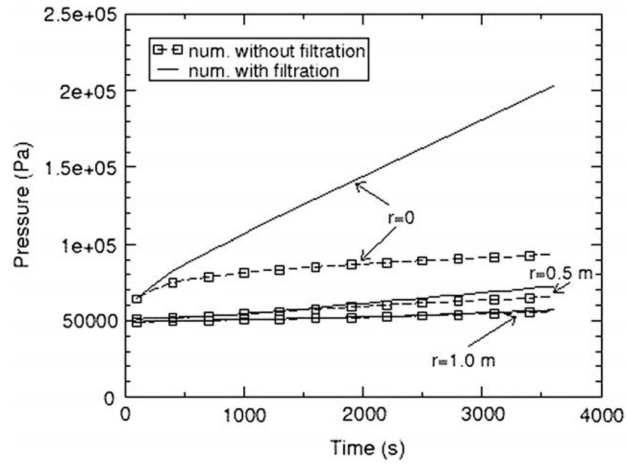

Fig. 10. Evolution of the pore pressure versus time at different locations (C/W = 0.42).

to be given at this point: the distance between the end of WG3 and the central axis of the tank is 0.4 m but it includes a part of the tube-a-manchette and the casing grout (approximately 5 cm). This remark tends to minimize the difference between the numerical and the AE statements. However, the AE method seems to detect the grout front in advance compared to the numerical results. An explanation could be that the collision of cement particles onto soil grains during injection engenders waves which are felt by the wave guides. In this case, the AE detection would not occur exactly at the arrival of grout upon the waves guides. Concerning the order of magnitude of the dispersion coefficients used in the simulation, they are inspired from the literature; they may not reflect perfectly the reality. The increase of AE activity detected by WG4 has been discussed previously.

Fig. 8 shows the concentration of the filtrated grout at times $t = 1500$ s, $t = 2500$ s and $t = 3500$ s. The concentration of the filtered species logically increases with time. Its evolution depends on the concentration of the transported grout which continuously spreads out within the medium during injection. Consequently, the region that contains filtered grout persistently extends but the concentration of filtrated grout remains relatively small even at $t = 3500$ s. The overpressure caused by filtration depends on the concentration of the filtrated species. Even if the Oberbeck–Boussinesq assumption is made, Darcy's law includes the permeability relation [Eq. (10)] that depends on χ.

The computed pore pressures for different r-coordinates (corresponding to the piezometer locations) at the altitude of the injection source are shown in Fig. 9. They continuously increase with time whatever the radial distance to the injection source. However, the pressure variations are very small for $r = 0.33$ m and $r = 0.66$ m. The difference of pressure between the beginning and the end of the injection is lower than 5 kPa for these two curves which are close to each other. This result matches the experimental observation since the overpressures measured by the piezometers range within 2 kPa. The experimental pressures measured by PZ1 and PZ2 during the injection through S6 are also displayed in Fig. 9. Note that during this injection the whole sand specimen is not saturated with water. In order to allow the comparison with the numerical results, the static piezometric level is consequently adjusted to represent the fully saturated condition used in the simulation. The experimental pressures are close to the computed values. The evolution of the pressure at the injection source (in $r = 0$) is largely more important. The amount of grout injected into soil is constantly increasing during the experiment. Thus, the injection pressure is expected to rise during the test (permeation grouting) aside from filtration effects that can also contribute to this trend. Note that the pore pressure is also influenced by variations of the fluid phase viscosity according to Eq. (11). The pressure measured at the outlet of the pump during injection S6 is plotted in Fig. 9 more as an indication than for a direct comparison with the injection pressure computed numerically. The experimental pressure in the tube-a-manchette, right behind a rubber sleeve, remains certainly difficult to correlate to the pressure computed in the medium at the injection source location.

The results presented in this paragraph tend to indicate that filtration has a relatively moderate impact on injection especially for radial distances greater than 0.33 m away from the injection source. This statement is supported by the low concentration of the filtered grout computed in the medium (Fig. 8) slightly away from the injection source. It does not mean that filtration is not occurring during the test but that either filtration is not a predominant phenomenon or its effect is limited to a region close to the injection source. As mentioned in [14], the C/W ratio of the grout has a major involvement in filtration processes. Therefore, to see whether the aforementioned statement can be accredited to the specific grout used during the tests, a simulation with a greater C/W ratio (C/W = 0.42) is performed. The overpressure only due to filtration is also regarded by comparing results obtained with and without filtration. Fig. 10 displays the pressure at different radial distances from the injection source as a function of time. The consequences of filtration on pore pressures are more important for regions near to the source. At a distance of 0.5 m, a slender difference between the curves with and without filtration is noticeable; this difference is large at the injection source. At the end of the experiment, the pore pressure in $r = 0$ is twice bigger than the pressure computed for C/W = 0.36 which by the way is approximately the same as the pressure without filtration for C/W = 0.42. According to the numerical results, the pressure in $r = 0$ is doubled as a results of filtration.

5. Conclusion

This article has presented experimental and numerical results about grouting of sandy soils. Successive injections were performed close to in-situ conditions by using a tube-a-manchette. They exposed fracturing patterns appearing at low injection speeds. These patterns were correlated to a drop of the injection pressure. The overpressures measured at different radial distances away from the injection source came out to be very small, i.e. inferior to 2 kPa. In the absence of anomalies during injection, the shape of a solidified bulb obtained after hardening of the grout was quasi spherical. A slight difference in the volume of solidified soil was noticed between an excavated bulb and a computation performed with a simple spherical model.

A simulation of the test was performed by using a model based on flow and transport in porous media equations that include filtration. This model depends on two filtration parameters that can be determined from one-dimensional injection tests. It also accounts for dispersion phenomena as well as density and viscosity effects. A finite element program was developed to solve the model equations. Special features of this program concern: (i) the MLS technique used to obtain a consistent velocity field (ii) the SUPG method that contributed to obtain a stable solution of the transport equation and (iii) the iterative methods (CG or BICCGS methods associated to a RILU preconditioner) utilized to accelerate the solving time. The program has been successfully tested on benchmarks and turned out to be suitable for the analysis of large scale problems over long time periods (coupled and nonlinear problems).

Despite of the difficulty to model in-situ injections, agreements between the simulation and the tests were observed on several points. The interstitial pressures away from the injection source were similar and the numerical results also showed low overpressures. An estimate of the size of a solidified bulb obtained numerically showed a small difference with the spherical model as previously noticed between the spherical model and an experimental bulb. The concentration of the filtered species remained relatively small during the simulation, especially away from the injection source. This observation combined to the low overpressures mentioned above tends to indicate that maybe the filtration was not a dominant phenomenon during this experiment or that its influence was restricted to a region near the injection source. To appraise the role of the grout composition on the filtration impact during injection, a simulation corresponding to a higher cement-to-water ratio was run. The overpressures computed away from the source were still small but the injection pressure was doubled at the end of the simulation as a result of filtration.

Acknowledgements

The authors would like to acknowledge Vsl-Intrafor-Soletanche and Euro Physical Acoustic companies for their participation in the experimental part of this work.

References

[1] Azzar G. Modélisation des injections de coulis de bentonite-ciment dans les sols. Thèse de doctorat, Ecole Nationale Supérieure d'Arts et Métiers, centre de Bordeaux; 1997.

[2] Bear J, Bachmat Y. Transport phenomena in porous media. In: Bear JJ, Corrapcioglu MY, editors. The basic equations in fundamentals of transport phenomena in porous media. Dordrecht: Martinus Nijhof; 1984.

[3] Bear J. Eight lectures on mathematical modelling of transport in porous media. In: Jacob Bear, Buchlin J-M. editors. Modelling and applications of transport phenomena in porous media; 1991.

[4] Bedrikovetsky P, Marchesin D, Shecaira F, Souza AL, Milanez PV, Rezende E. Characterisation of deep bed filtration system from laboratory pressure drop measurements. J Petrol Sci Eng 2001;32:167–77.

[5] Benhamou. Comportement rhéologique des coulis de liants hydrauliques ultrafins destinés à l'injection. Thèse de doctorat, Centre de Géologie de l'Ingénieur, Ecole Nationale Supérieure des Mines de Paris; 1994.

[6] Bouchelaghem F, Vulliet L. Mathematical and numerical filtration–advection–dispersion model of miscible grout propagation in saturated porous media. Int J Numer Anal Geomech 2001;25:1195–227.

[7] Bouchelaghem F, Vulliet L. Real-scale miscible grout injection experiment and performance of advection–dispersion–filtration model. Int J Numer Anal Geomech 2001;25:1149–73.

[8] Bouchelaghem F. Modélisation de la propagation d'un coulis d'injection dans un milieu granulaire. PhD thesis, Lausanne, Switzerland; 2001.

[9] Bouchelaghem F. Two large-scale injection experiments, and assessment of the advection–dispersion–filtration model. Geotechnique 2002;5(9):667–82.

[10] Brooks AN, Hughes TJR. Streamline upwind/Petrov–Galerkin formulations for convection dominated flows with particular emphasis on the incompressible Navier–Stokes equations. Comput Methods Appl Mech Eng 1982;32:199–259.

[11] Cambefort H. Pression et débit d'injection avec le tube à manchette. Annales de l'Institut Technique du Bâtiment et des travaux publics. Série: Sols et Fondations 214. NO 500; 1992.

[12] Choo C-U, Tien C. Analysis of the transient behavior of deep bed filtration. J Colloid Interf Sci 1995;169:13–33.

[13] Chupin O. Ecoulement et transport couplés en milieu poreux saturé: application à l'injection des sols. PhD thesis from Ecole Centrale de Nantes, France; 2005. 188pp.

[14] Chupin O, Saiyouri N, Hicher P-Y. The effects of filtration on the injection of cement-based grouts in sand columns. Transp Porous Med 2008;72:227–40.

[15] Cividini A. A study of low pressure grouting of granular soils. In: Smith, Carter, editors. Developments in theoretical geomechanics. Rotterdam: Balkema; 2000. p. 525–46.

[16] Dano C, Hareb H, Hicher P-Y. Characterization of Loire river sand in the small strain domain using new bender–extender elements. In: 16th ASCE engineering mechanics conference, University of Washington, Seattle 16–18 july; 2003.

[17] Diersch H-JG, Kolditz O. Variable-density flow and transport in porous media: approaches and challenges. Adv Water Resour 2002;25:899–944.

[18] Elder JW. Transient convection in a porous medium. J Fluid Mech 1967;27:609–23.

[19] Eriksson M, Stille H, Anderson J. Numerical calculations for grout spread with account for filtration and varying aperture. Tunn Undergr Space Technol 2000;15:353–64.

[20] Hassanizadeh M, Gray WG. General conservation equations for multi-phase systems: 1. Averaging procedure. Adv Water Resour 1979;2:131–44.

[21] Hassanizadeh M. Derivation of basic equations of mass transport in porous media Part 1. Macroscopic balance laws. Adv Water Resour 1986;9:196–206.

[22] Henry HR. Interfaces between salt water and fresh water in coastal aquifers. US Geological survey water supply paper 1613-C, sea water in coastal aquifers: C35-C70; 1964.

[23] Herzig JP, Leclerc DM, LeGoff P. Flow of suspensions through porous media – application to deep bed filtration. Ind Eng Chem 1970;62(5):8–35.

[24] Homna S. Finite element analysis of the injection and distribution of the chemical grout injection in soil, PhD thesis, the University of Wisconsin-Milwaukee; 1984.

[25] Iwasaki T. Some notes on sand filtration. J Am Water Works Ass 1937;29:1591–602.

[26] Katzenbach R, Boley C, Festag G. Advanced models for computing the propagation of grouting material. In: Rathmayer H, Helsinki, editors. Proceedings of the fourth international conference on ground improvement geosystems, Finland, June 7–9; 2000.

[27] Kim YS, Whittle A. Filtration in a porous granular medium: 1. Simulation of pore scale particle deposition and clogging. Transp Porous Med 2006;65:53–87.

[28] Kim YS, Whittle A. Filtration in a porous granular medium: 2. Application of bubble model to 1-D column experiments. Transp Porous Med 2006;65:309–35.

[29] Kutzner C. Grouting of rock and soil. Rotterdam: A.A Balkema, Brookfield; 1996.

[30] Langtangen HP. Computational partial differential equations: numerical methods and Diffpack programming. Berlin Heidelberg: Springer-Verlag; 1999.

[31] McDowell-Boyer LM, Hunt JR, Sitar N. Particle transport through porous media. Water Resour Res 1986;22(13):1901–21.

[32] Rege SD, Fogler HS. A network model for deep bed filtration of solid particles and emulsion drops. AIChE J 1988;34(11):1761–72.

[33] Saada Z, Canou J, Dormieux L, Dupla JC, Maghous S. Modelling of cement suspension flow in granular porous media. Int J Numer Anal Methods Geomech 2004;29:691–711.

[34] Sharma MM, Yortsos YC. Transport of particulate suspensions in porous media: model formulation. AIChE J 1987;33:1636–43.

[35] Tamura M, Goto T, Ogino T, Shinizu K. Injection with ultra-fine cement into fine sand layer. In: Proceedings of the fourth international offshore and polar engineering conference, Osaka, Japan, April 10–15; 1994. p. 567–71.

[36] Tarafdar S, Dey A, Gupta BS. A multiple state stochastic model for deep bed filtration. Chem Eng Technol 1992;15(1):44–50.

[37] Tarumi H, Sekine E. Study of grouting patterns based on pressure–speed relations and pressure–time charts. QR RTRI 1993;34:255–62.

[38] Zienkiewicz OC, Taylor RL. The finite element method, vol. 2. 5th ed. Butterworth-Heinemann; 1982.